Nonlocal neoclassical transport in tokamak and spherical torus experiments

W. X. Wang, G. Rewoldt, W. M. Tang, F. L. Hinton,[a] J. Manickam, L. E. Zakharov, R. B. White, and S. Kaye
Princeton Plasma Physics Laboratory, Princeton University P.O. Box 451, Princeton, New Jersey 08543

(Received 29 March 2006; accepted 5 July 2006; published online 4 August 2006)

Large ion orbits can produce nonlocal neoclassical effects on ion heat transport, the ambipolar radial electric field, and the bootstrap current in realistic toroidal plasmas. Using a global δf particle simulation, it is found that the conventional local, linear gradient-flux relation is broken for the ion thermal transport near the magnetic axis. With regard to the transport level, it is found that details of the ion temperature profile determine whether the transport is higher or lower when compared with the predictions of standard neoclassical theory. Particularly, this nonlocal feature is suggested to exist in the National Spherical Torus Experiment (NSTX) [M. Ono, S. M. Kaye, Y.-K. M. Peng *et al.*, Nucl. Fusion **40**, 557 (2000)], being consistent with NSTX experimental evidence. It is also shown that a large ion temperature gradient can increase the bootstrap current. When the plasma rotation is taken into account, the toroidal rotation gradient can drive an additional parallel flow for the ions and then additional bootstrap current, either positive or negative, depending on the gradient direction. Compared with the carbon radial force balance estimate for the neoclassical poloidal flow, our nonlocal simulation predicts a significantly deeper radial electric field well at the location of an internal transport barrier of an NSTX discharge. © *2006 American Institute of Physics*.
[DOI: 10.1063/1.2244532]

I. INTRODUCTION

In a toroidal plasma, turbulence driven transport usually well exceeds the neoclassical level. To control and even fully suppress turbulence fluctuations is one of the major goals of fusion research in experiments. If turbulence is suppressed, toroidal plasma transport is governed by the universal Coulomb collision process. The associated neoclassical dynamics accounts for the irreducible minimum of dissipation in toroidal systems. Indeed, many present advanced tokamak experiments are able to reduce transport, particularly in the ion channel, to the neoclassical level, and thus to achieve improved confinement.

In order to assess the confinement properties and performance of toroidal devices, the neoclassical transport level is routinely compared with experimental results. Therefore, it is important to accurately calculate the neoclassical dynamics that set the irreducible minimum level of transport in such systems. Moreover, the bootstrap current and equilibrium radial electric field, which, in general, play important roles in affecting the overall plasma confinement and performance of toroidal systems, are essentially determined by neoclassical dynamics. While standard neoclassical theory[1,2] has been well developed, there remain significant unresolved nonlocal physics issues in tokamaks, including spherical torus devices such as the National Spherical Torus Experiment (NSTX).[3] In NSTX plasmas, typical features that violate the basic assumptions of most local theories include the large orbit size compared to the local minor radius and/or plasma equilibrium scale length, low aspect ratio and low magnetic field, large trapped particle fraction (even approaching ~100%), large toroidal rotation with strong shear, a large ion gyroradius,[4] etc. Another important issue that is missing in most theories is the self-consistent determination of the (equilibrium) electric field that is established to maintain transport ambipolarity.[5] Also, the neoclassical fluxes are predicted to be independent of the radial electric field. This equilibrium electric field may change neoclassical transport by changing the particle orbits.[5,6] The sheared equilibrium electric field is also believed to play an important role in determining the turbulence level and associated transport both locally and globally. When these effects are properly taken into account, it is obviously of great interest to examine the nonlocal neoclassical properties, such as the ion thermal transport and the bootstrap current, in experimental situations. This is our primary purpose in this paper.

The methodology used for this study is particle-in-cell (PIC) simulation using a δf method. The δf simulation technique was previously used for studying plasma microturbulence[7] and later applied to neoclassical transport studies.[8,9] Recently, we have developed a generalized global PIC neoclassical code GTC-Neo.[10] Unlike the standard neoclassical analysis, which solves the drift kinetic equations locally (on a single magnetic surface), based on a small orbit width expansion, for collision driven fluxes, viscosity and bootstrap current, GTC-Neo numerically solves an initial value problem for the drift kinetic equations globally, from the magnetic axis to the plasma boundary with appropriate boundary conditions, and with full particle drift orbit dynamics. Moreover, critically, the large scale ambipolar electric field is also consistently calculated by solving the Poisson equation.[5] Our first-principles based simulation also incorporates important realism of tokamak experiments. It is inter-

[a]Also at General Atomics, San Diego, California 92186-5608.

faced with TRANSP,[11] a widely used experimental data analysis software tool for specifying experimental plasma profiles of temperature, density and toroidal angular velocity, and corresponding magnetohydrodynamic (MHD) equilibria numerically calculated by various codes, including JSOLVER[12] and ESC.[13] The collision-driven particle, heat and angular momentum fluxes, bootstrap current, equilibrium electric field, etc., are calculated, given the plasma profiles of density $n(r)$, temperature $T(r)$, and toroidal rotation angular velocity $\omega_t(r)$, and the equilibrium geometry. At present, the GTC-Neo calculation only includes a single (hydrogenic) ion species, but we plan to add impurity species in future work. In general, the verification and validation of this new computational model with respect to analytic theory and experimental observations proved to be very encouraging.

In standard neoclassical transport theory, the particle and heat transport show local and diffusive features. There exists a Fick's law type linear relation between the thermodynamic forces (such as local plasma gradients of pressure, temperature, etc.) and driven transport fluxes. The obtained transport coefficients are in accord with heuristic arguments based on random walk diffusion processes, properly taking into account toroidal effects on particle radial excursion (step size), and effective collision frequency. In anomalous transport analysis, an analogous mixing-length argument has been employed to estimate the turbulence driven transport diffusivity. Apparently, the local and diffusive transport requires that the radial excursion, which essentially is the orbit width of trapped particles here, is small compared to the plasma equilibrium scale length or/and system size (typically, the local minor radius). Generally, the nonlocal effects associated with large orbit size may introduce the dependence of transport fluxes on higher order radial derivatives of the plasma profiles and on the shape of the profiles, rather than a unique relation to the first derivative (plasma gradients). In the region near the magnetic axis, particle drift orbits change topologically, which causes problems for conventional neoclassical theory. It is found that the conventional linear gradient-flux relation is broken for ion heat transport in the region near the magnetic axis. Our simulations suggest that neoclassical ion transport in NSTX plasmas exhibits a nonlocal nature, which is consistent with NSTX experimental evidence. For NSTX plasmas, the comparison of our simulation results for ion heat transport to experiment is more meaningful, as it is believed that the energy loss in the ion channel is often dominated by neoclassical mechanisms. With regard to the bootstrap current, a noninductive current directly associated with the existence of trapped particles in toroidal geometry, it is found that sheared toroidal rotation and steep temperature gradients can modify the standard neoclassical results. Both can be attributed to the finite ion orbit effects on the ion parallel flow velocity. The radial electric field calculated from our simulation is compared with the estimate using the radial force balance relation with experimentally measured profiles of pressure and toroidal rotation angular velocity and the neoclassical poloidal flow velocity. A significant difference in E_r is observed in the region of an internal transport barrier with a steep ion temperature gradient.

The remainder of this paper is organized as follows: In Sec. II, the simulation model and the δf method are described. The benchmark simulations against the standard neoclassical theory in large aspect ratio circular concentric geometry with a small orbit size are presented in Sec. III. In Sec. IV, the result for nonlocal ion heat transport is reported and discussed, and compared with NSTX measurements. In Sec. V, the results for the bootstrap current in toroidally rotating plasmas and the corrections due to a large temperature gradient are reported and discussed. The simulated ambipolar neoclassical electric field is compared with the radial force balance relation for NSTX plasmas in Sec. V. A summary is given in Sec. VI.

II. SIMULATION MODEL, δf METHOD, AND BENCHMARKS

Our global drift kinetic simulation solves an initial value problem, following a rotating toroidal plasma to a neoclassical steady state. It uses a δf particle in cell simulation method.

A. Lowest order distribution of large-rotation plasma f_0

In this section, we first follow the standard small orbit analysis[14,15] to give a lowest order distribution f_0 for a rotating plasma. This will provide a foundation or guideline as to the best way to separate δf from the full distribution function f.

We start from the ion drift kinetic equation,

$$\frac{\partial f}{\partial t} + (\mathbf{v}_\parallel + \mathbf{v}_D + \mathbf{v}_E)\cdot\nabla f - \frac{e}{m_i}(\mathbf{v}_\parallel + \mathbf{v}_D)\cdot\nabla\Phi\frac{\partial f}{\partial \varepsilon} = C_{ii}[f,f], \tag{1}$$

where the independent velocity variables are the magnetic moment μ and kinetic energy $\varepsilon \equiv v_\parallel^2/2 + \mu B$ with B the magnitude of the magnetic field and $v_\parallel$ the parallel velocity, Φ is the electric potential, $\mathbf{v}_D$ and $\mathbf{v}_E$ are the ∇B drift and the $\mathbf{E}\times\mathbf{B}$ drift, respectively, C_{ii} is the ion-ion collision operator, and e and m_i are ion charge and mass, respectively.

The small parameter in neoclassical analysis is the ratio of the ion poloidal gyroradius to the gradient scale length of equilibrium quantities: $\epsilon \equiv \rho_{i\theta}/L \ll 1$. The distribution function and the electric field are expanded as follows:

$$f = f_0 + f_1 + \cdots, \quad \Phi = \Phi_{-1} + \Phi_0 + \cdots. \tag{2}$$

It is noted that the leading order for the electric field is set to be -1, one order larger than the conventional drift ordering. This corresponds to the assumption of a large flow velocity comparable to the thermal velocity. This large toroidal rotation is indeed driven in tokamak experiments, for example, by neutral beam heating. With the additional assumption $\partial/\partial t \sim \epsilon^2 \nu_{ii}$, which specifies the time scale for changing plasma profiles due to neoclassical transport, we obtain the lowest order equation,

$$-\frac{e}{m_i}\mathbf{v}_\parallel\cdot\nabla\Phi_{-1}\frac{\partial f_0}{\partial\varepsilon}=0, \tag{3}$$

which tells us simply that the lowest order potential is a flux function $\Phi_{-1}(\psi)$, with ψ a flux label, or that the leading order electric field is in the radial direction.

The next order equation is

$$\left(\mathbf{v}_\parallel+\frac{\hat{b}\times\nabla\Phi_{-1}}{B}\right)\cdot\nabla f_0-\frac{e}{m_i}\mathbf{v}_D\cdot\nabla\Phi_{-1}\frac{\partial f_0}{\partial\varepsilon}-\frac{e}{m_i}\mathbf{v}_\parallel\cdot\nabla\Phi_0\frac{\partial f_0}{\partial\varepsilon}=C_{ii}[f_0,f_0]. \tag{4}$$

This equation can be largely simplified by transforming velocity variables (μ,ε) to (μ,ε') with

$$\varepsilon'=\varepsilon''+\frac{e}{m_i}\tilde{\Phi}_0-\frac{u_\parallel^2}{2},$$

where $\varepsilon''\equiv v_\parallel'^2/2+\mu B$, $v_\parallel'\equiv v_\parallel-u_\parallel$, $\tilde{\Phi}_0\equiv\Phi_0-\langle\Phi_0\rangle$. The shift velocity $u_\parallel\equiv-(cI/B)d\Phi_{-1}/d\psi_p$, where c is the light speed, ψ_p is the poloidal flux, and $I=RB_\zeta$, with R the major radius and B_ζ the toroidal component of the magnetic field $\mathbf{B}$. Actually, this corresponds to a transformation from the lab frame to a toroidally rotating frame with rotation angular velocity $\omega(\psi_p)=(B/I)u_\parallel$, and $\varepsilon'$is the particle energy in the rotating frame. In the rotating frame, Eq. (4) is simplified to

$$\mathbf{v}_\parallel'\cdot\nabla f_0=C_{ii}[f_0,f_0]. \tag{5}$$

The solution of Eq. (5) is a Maxwellian, i.e., a shifted Maxwellian in the lab frame:

$$f_0=f_{\mathrm{SM}}=n\left(\frac{m_i}{2\pi T_i}\right)^{3/2}e^{-\frac{m_i}{T_i}[(1/2)(v_\parallel-u_\parallel)^2+\mu B]}, \tag{6}$$

where the density $n(\psi,\theta)=N(\psi)e^{m_iu_\parallel^2/2T_i-e\tilde{\Phi}_0/T_i}$, depending on both ψ and the poloidal angle θ, and the temperature $T_i=T_i(\psi)$.

B. Basic equations for ions and ambipolar electric field

Based on the lowest order solution, Eq. (6), we decompose the ion guiding center distribution: $f=f_{\mathrm{SM}}+\delta f$. Note that for the δf simulation, the decomposition of the distribution function does not necessarily have to be strict as long as δf is smaller than the total f. However, a smaller δf will reduce the noise in the simulation. The distribution δf obeys the following drift kinetic equation:

$$\frac{\partial\delta f}{\partial t}+(\mathbf{v}_\parallel+\mathbf{v}_d)\cdot\nabla\delta f-\frac{e}{m_i}(\mathbf{v}_\parallel+\mathbf{v}_d)\cdot\nabla\Phi\frac{\partial\delta f}{\partial\varepsilon}=-(\mathbf{v}_\parallel+\mathbf{v}_d)\cdot\nabla f_{\mathrm{SM}}+\frac{e}{m_i}(\mathbf{v}_\parallel+\mathbf{v}_d)\cdot\nabla\Phi\frac{\partial f_{\mathrm{SM}}}{\partial\varepsilon}+C_{ii}^l(\delta f), \tag{7}$$

where the guiding center drift velocity $\mathbf{v}_d$ includes both the ∇B and $\mathbf{E}\times\mathbf{B}$ drifts: $\mathbf{v}_d=\mathbf{v}_D+\mathbf{v}_E$. The linearized ion-ion collision operator $C_{ii}^l(\delta f)\equiv C_{ii}[\delta f,f_{\mathrm{SM}}]+C_{ii}[f_{\mathrm{SM}},\delta f]$ is calculated in terms of linear collisions with a Maxwellian background[8,9,16] in the local moving frame in the rotating plasma. It should be mentioned that this simulation model is not limited to a small orbit size, even though δf is separated based on the lowest order solution, Eq. (6), of the small orbit analysis. The finite orbit physics is included by the $\mathbf{v}_d\cdot\nabla\,\delta f$ term on the left hand side of Eq. (7), along with its radially global solution. Actually, the only approximation in Eq. (7) relative to the original drift kinetic equation (1) is the neglect of the nonlinear collision term $C_{ii}[\delta f,\delta f]$. Another important feature of the model is the inclusion of a self-consistent ambipolar electric field. The equation for the ambipolar potential Φ in general geometry is,[5] from Poisson's equation and the continuity equations,

$$\left(\langle|\nabla r|^2\rangle+4\pi m_ic^2\left\langle\frac{n|\nabla r|^2}{B^2}\right\rangle\right)\frac{\partial^2\Phi}{\partial t\,\partial r}=4\pi e\Gamma_i^r, \tag{8}$$

where r is a radial coordinate (flux label) and the angular brackets denote a flux surface average. On the right hand side, $e\Gamma_i^r$ is the radial current of ion guiding centers, including both self-collision driven neoclassical diffusion and polarization currents (associated with toroidal geometry): $e\Gamma_i^r\equiv e\langle\int d^3v(\mathbf{v}_d\cdot\nabla r)\delta f\rangle$. The unlike particle collisions do not produce any radial current because they drive particle fluxes that are intrinsically ambipolar. The second term on the left hand side is the classical polarization current associated with particle gyromotion with a temporally varying electric field, presented for a general magnetic field. In axisymmetric geometry, the electron radial currents (both classical polarization current and the neoclassical guiding center current) are much smaller than the ion currents due to the small mass ratio. Thus, electron dynamics has a very minor role in determining the ambipolar electric field and is neglected in the ion simulation. However, this is not true for nonaxisymmetric geometry, such as in a stellarator, where the lowest order particle fluxes driven by unlike-particle collisions are not automatically ambipolar. For an initial toroidal plasma, a shifted Maxwellian with either given profiles or experimental profiles for $\langle n(r,\theta)\rangle$, $T_i(r)$ and $\omega_t(r)$ are prescribed for the ions. The initial potential and parallel velocity are determined by $d\Phi(0)/dr=-(d\psi_p/dr)(\omega_t/c)$ and $u_\parallel(0)=(I/B)\omega_t$. In the present study, the potential variation on a magnetic surface is neglected, which may be important for calculating angular momentum transport.[17] The rotating ions are followed to reach a neoclassical steady state on a time scale of a few ion collision times in a low collisionality regime or a few transit times in a high collisionality regime, which usually is much shorter than the transport time scale.

C. Model for electrons

Generally, electron and ion dynamics interact with each other via the Coulomb collisions and the electric field. For axisymmetric geometry, however, electrons and ions can be effectively decoupled by taking into account the small mass ratio approximation. As we discussed above, the equilibrium electric field can be determined by the ion dynamics, neglecting electrons. The electric field evolves due to collisional angular momentum transport, which occurs on a transport time scale longer than that of the thermal transport.[18]

This allows us to use, for the electron simulation, a quasi-steady state electric field that is obtained from the ion simulation. Again, due to the small mass ratio, electron-ion collisions are essentially a pitch angle scattering process, and it is a good approximation to use the Lorentz gas collision model without taking into account the details of the ion distribution. In this way, the electron simulation can be decoupled from ions. Because of the friction force between electrons and the ions, electrons rotate with essentially the same velocity as ions. We decompose the electron distribution: $f_e=f_{\mathrm{SM}}+\delta f_e$ with $f_{\mathrm{SM}}=n(m_e/2\pi T_e)^{3/2}e^{-(m_e/T_e)[(v_\parallel-u_\parallel)^2/2+\mu B]}$, which contains a parallel flow that is the same as that for ions. The drift kinetic equation for the distribution δf_e is

$$\frac{\partial \delta f_e}{\partial t}+(\mathbf{v}_\parallel+\mathbf{v}_d)\cdot\nabla\delta f_e-\frac{e_e}{m_e}(\mathbf{v}_\parallel+\mathbf{v}_d)\cdot\nabla\Phi\frac{\partial \delta f_e}{\partial \varepsilon}$$
$$=-(\mathbf{v}_\parallel+\mathbf{v}_d)\cdot\nabla f_{\mathrm{SM}}+\frac{e_e}{m_e}(\mathbf{v}_\parallel+\mathbf{v}_d)\cdot\nabla\Phi\frac{\partial f_{\mathrm{SM}}}{\partial \varepsilon}$$
$$+C^l_{ee}(\delta f_e)+C_{ei}(\delta f_e), \tag{9}$$

where C_{ei} is the e-i collision operator that actually uses the Lorentz pitch angle scattering model in the simulation

$$C_{ei}(\delta f_e)=\frac{\nu_e}{2}\frac{\partial}{\partial\lambda}(1-\lambda^2)\frac{\partial}{\partial\lambda}\delta f_e,$$

with $\lambda=v_\parallel/v$ the pitch angle variable (the cosine of particle pitch angle) and ν_e the collision frequency, and C^l_{ee} the linear electron-electron collision operator, which has the same form as C^l_{ii}, and e_e and m_e are the electron charge and mass, respectively. The electron distribution is solved for in the ion rest frame independently, with the equilibrium electric field imported from the results of the ion simulation.

One important issue for electron simulations is the calculation of the total bootstrap current (electrons + ions) in terms of δf_e:

$$\langle j_b B\rangle=-e\left\langle B\int v_\parallel\,\delta f_e\,d^3v\right\rangle. \tag{10}$$

Our δf simulation uses a two-weight algorithm,[9] incorporating a noise reduction algorithm,[19] which is shown to rigorously reproduce the drift kinetic equations.[10]

D. Particle guiding center motion–Lagrangian equations

A particle simulation requires an accurate and efficient calculation of particle motion. Simulation particles are followed along the guiding center trajectories using Lagrangian equations:[20,21]

$$\begin{vmatrix}\dot\rho_\parallel\\ \dot r\\ \dot\theta\\ \dot\zeta\end{vmatrix}=\begin{vmatrix}0&0&\frac{a_{22}}{A}&-\frac{a_{12}}{A}\\ 0&0&-\frac{a_{21}}{A}&\frac{a_{11}}{A}\\ \frac{a_{22}}{A}&-\frac{a_{21}}{A}&0&-\frac{B_r}{A}\\ -\frac{a_{12}}{A}&\frac{a_{11}}{A}&\frac{B_r}{A}&0\end{vmatrix}\cdot\begin{vmatrix}\frac{\partial H}{\partial\rho_\parallel}\\ \frac{\partial H}{\partial r}\\ -\frac{\partial H}{\partial\theta}\\ -\frac{\partial H}{\partial\zeta}\end{vmatrix}, \tag{11}$$

which are normalized by the particle gyrofrequency $\Omega_0=eB_0/mc$, for time, with a reference magnetic field B_0, and l_0 for length. Here, (r,θ,ζ) denote general toroidal coordinates with r a flux label; $\rho_\parallel=v_\parallel/B$ is the parallel gyroradius, $H=\rho_\parallel^2B^2/2+\mu B+\Phi$ is the guiding center Hamiltonian, $a_{11}=B_\theta$, $a_{12}=\mathcal{J}(B^\zeta+\rho_\parallel j^\zeta)$, $a_{21}=B_\zeta$, $a_{22}=-\mathcal{J}(B^\theta+\rho_\parallel j^\theta)$, $A=a_{11}a_{22}-a_{12}a_{21}=-\mathcal{J}(B^2+\rho_\parallel\mathbf{B}\cdot\mathbf{j})$, and the Jacobian $\mathcal{J}=(\nabla r\times\nabla\theta\cdot\nabla\zeta)^{-1}$. The relevant covariant and contravariant components of $\mathbf{B}$ and the current $\mathbf{j}$ are defined as

$$\mathbf{B}=B_r\nabla r+B_\theta\nabla\theta+B_\zeta\nabla\zeta$$
$$=\mathcal{J}B^\theta\nabla\zeta\times\nabla r+\mathcal{J}B^\zeta\nabla r\times\nabla\theta,$$

$$\mathbf{j}=\nabla\times\mathbf{B}=\mathcal{J}j^\theta\nabla\zeta\times\nabla r+\mathcal{J}j^\zeta\nabla r\times\nabla\theta.$$

Compared to the widely used Hamiltonian equations that require the construction of canonical variables, which are complicated forms in general geometry,[21] the Lagrangian equations are suitable for any generalized flux coordinates.

In principle, GTC-Neo uses arbitrary flux coordinates. The radial coordinate is r defined as $r=\sqrt{\psi/\psi_e}$, where ψ and ψ_e are the toroidal flux and its value on the plasma boundary, respectively. A poloidal angle θ_E with an approximately equal arclength is usually used in the simulations. It is defined in terms of cylindrical coordinates (R, Z) as

$$R(r,\theta_E)=\sum_m R_m(r)e^{im\theta_E},\quad Z(r,\theta_E)=Z_0(r)+Z_1(r)\sin\,\theta_E.$$

This coordinate system allows a uniform grid in the poloidal direction, a better representation of the numerical equilibrium for high β (ratio of plasma pressure to magnetic pressure), strongly shaped plasmas such as NSTX, and then increased accuracy of interpolation for equilibrium quantities. Multidimensional spline interpolation is used to obtain equilibrium quantities at any spatial location. The global simulation domain covers the entire torus, radially from the magnetic axis to the separatrix. A two-dimensional (2-D) mesh with uniform Δr and $\Delta\theta_E$ is used for axisymmetric geometry.

E. Benchmark simulations

The drift kinetic simulation is rigorously benchmarked with neoclassical theory in the limit of large aspect ratio circular concentric geometry with a small orbit size. The benchmark results are presented later. All test simulations are carried out with aspect ratio $R_0/a=10$.

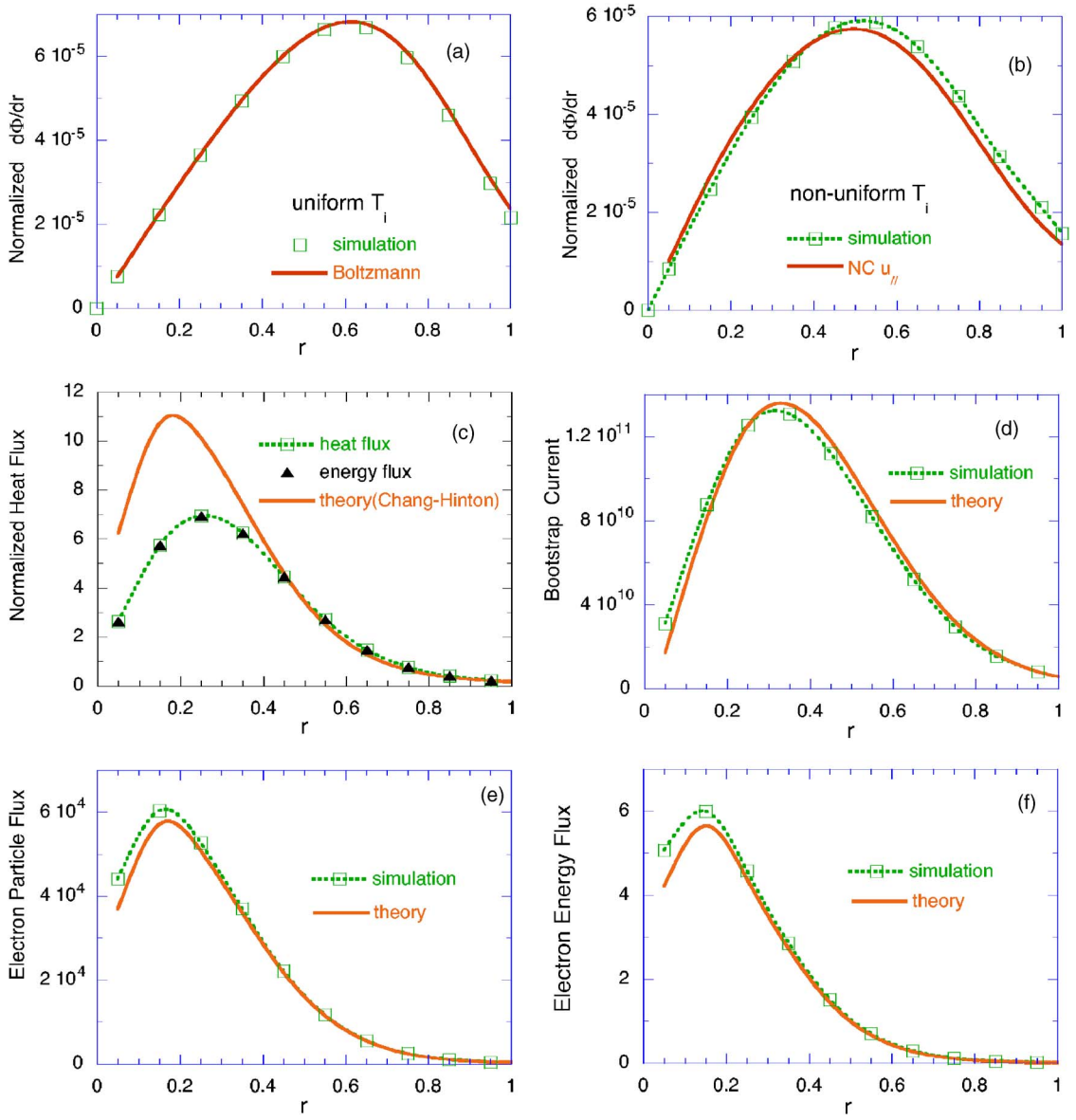

FIG. 1. (Color online) Benchmark results of global GTC-Neo simulation against standard neoclassical (local) theory in a large aspect ratio circular concentric geometry limit (aspect ratio $R_0/a=10$): (a) radial electric field with uniform ion temperature compared with Eq. (12); (b) E_r with nonuniform temperature compared with neoclassical theory of ion parallel flow; (c) ion heat flux compared with the Chang-Hinton formula; (d) total (electron+ion) bootstrap current; (e) electron heat flux; and (f) electron particle flux.

We first discuss the equilibrium radial electric field. In a toroidal plasma with uniform temperature, there exists a Boltzmann-like condition that relates the equilibrium electric field to the density gradient:[5]

$$\ln \frac{n_i}{n_a} + \frac{e\Phi}{T_i} = b\psi, \tag{12}$$

where b is a constant related to the edge toroidal rotation and n_a is a constant. In Fig. 1(a), the equilibrium electric field of a simulation with uniform temperature is compared with the Boltzmann relation and very good agreement is seen. In the case of nonuniform temperature, the simulation result for the electric field is compared in Fig. 1(b) with the one evaluated in terms of the standard neoclassical expression for the ion parallel flow velocity:

$$u_{i\|} = \frac{I}{\Omega_i \psi'} \frac{T_i}{m_i} \left((k-1) \frac{\partial \ln T_i}{\partial r} - \frac{\partial \ln n_i}{\partial r} - \frac{e}{T_i} \frac{\partial \Phi}{\partial r} \right), \tag{13}$$

where k is a function of ion collisionality. Figure 1(c) shows the ion heat flux and energy flux, compared with the widely used Chang-Hinton formula.[22] Good agreement between the simulation and the theory is obtained in the outer region of the torus, but not in the inner region close to the magnetic axis. The discrepancy near the magnetic axis arises from the important finite orbit physics, and we will come back to this issue in Sec. III. Actually, the simulation agrees with the theory in the region close to the magnetic axis only when the finite orbit effect is artificially suppressed by neglecting the drift terms $\mathbf{v}_d \cdot \nabla \delta f$ and $(\mathbf{v}_d \cdot \nabla \Phi)\, \partial \delta f / \partial \varepsilon$ on the left hand side of Eq. (7).[5]

The radial profile of the bootstrap current is plotted in Fig. 1(d) and compared with the result of neoclassical theory, which can be written as

$$\langle j_b B\rangle = -L_{31}\left(\frac{\partial}{\partial\psi}P_e + \frac{\partial}{\partial\psi}P_i\right) - L_{32}^{e}\frac{\partial}{\partial\psi}\ln T_e - L_{32}^{i}\frac{\partial}{\partial\psi}\ln T_i, \tag{14}$$

with L_{31}, L_{32}^{e}, and L_{32}^{i} the standard bootstrap current coefficients.[2] This total bootstrap current includes contributions of both ions and electrons, which are usually of a roughly equal amount. The simulated bootstrap current agrees well with the theory over the entire minor radius except for the area close to the magnetic axis, where the current is small. Good agreement is also obtained for the electron particle flux and energy flux, as shown in Figs. 1(e) and 1(f). It is noticed that much better agreement for electron fluxes is shown near the magnetic axis, compared to the results for ion energy (heat) flux [Fig. 1(c)]. This difference is caused by the different orbit sizes between electrons and ions, and demonstrates the influence of the large orbit effect.

F. Discussion of self-collision driven particle flux

Note that the energy flux Q is the sum of the heat flux q and the convective energy flux carried by the particle flux Γ: $Q=q+(5/2)T\Gamma$. In Fig. 1(c) the ion energy flux equals the heat flux, indicating that the self-collision driven ion particle flux is zero. This result is nontrivial in the sense that it is obtained only when the self-consistent ambipolar electric field is used. The following discussion addresses the self-collision driven particle flux in toroidal systems. We consider and compare two dynamic systems (or two simulations) that follow the evolution of Maxwellian ions, in terms of the drift kinetic equation with only ion-ion collisions, to a neoclassical steady state. The steady state is known to be characterized by a parallel flow given by Eq. (13). Initially ions as a whole have no toroidal rotation, i.e, zero angular momentum and parallel velocity. In the case with no self-consistent ambipolar electric field, a parallel flow develops for the neoclassical steady state, which satisfies Eq. (13) with $\partial\Phi/\partial r=0$; or, equivalently, a nonzero toroidal rotation (angular momentum) is developed. This clearly indicates that without the self-consistent electric field, a net angular momentum is generated in the simulation system. To relate the nonzero ion-ion particle flux to the angular momentum generation in this system, we examine the angular momentum transport equation,

$$\frac{\partial U}{\partial t} + \frac{1}{\mathcal{V}'}\frac{\partial}{\partial r}(\mathcal{V}'\Pi_i) = \Gamma_i^{\psi_p}, \tag{15}$$

where the angular momentum density is $U=\langle\int d^3v(Iv_\parallel/\Omega_i)\delta f\rangle$, the angular momentum flux is $\Pi_i=\langle\int d^3v(Iv_\parallel/\Omega_i)(\mathbf{v}_d\cdot\nabla r)\delta f\rangle$, $\Gamma_i^{\psi_p}$ is the ion particle flux with respect to ψ_p, and $\mathcal{V}'=d\mathcal{V}/dr$ with $\mathcal{V}$ the volume enclosed by a flux surface r. This equation is obtained exactly from Eq. (7) by taking the flux-surface averaged moment of $Iv_\parallel/\Omega_i$. For the zero collision frequency boundary condition used in the simulations, no angular momentum flux is driven on the boundary. Thus, the self-collision driven ion flux $\Gamma_i^{\psi_p}$, working as a source in Eq. (15), is solely responsible for the buildup of the angular momentum. This explains the generation of an ion-ion flux in the simulation system without a self-consistent electric field. On the other hand, when a self-consistent electric field is included, angular momentum is indeed conserved. Equation (13) is satisfied by the establishment of a radial electric field. In this case momentum is conserved and ambipolarity is restored with a vanishing ion-ion flux.

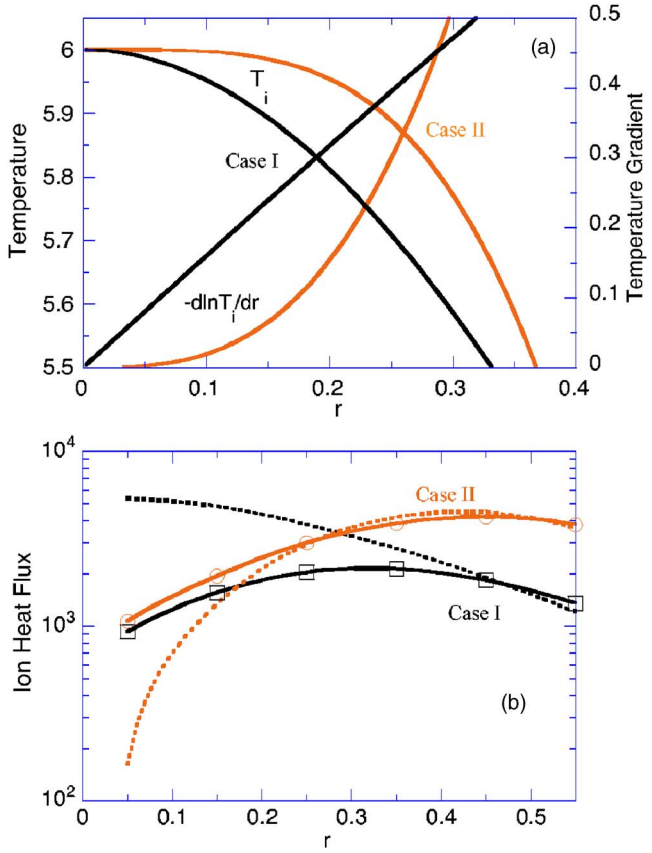

FIG. 2. (Color online) Simulated ion heat fluxes versus r (the near magnetic axis) compared with local transport theory prediction (dotted lines from the Chang-Hinton formula). Simulations use a numerical MHD equilibrium of circular cross section with $R_0/a=5$, and two specified pressure profiles.

III. NONLOCAL ION THERMAL TRANSPORT

The most interesting result found from our simulations is the nonlocal nature of the ion thermal transport near the magnetic axis. Here, we first use two simulations to illustrate that the ion thermal transport is decoupled from the local plasma parameters. The two simulations are carried out using identical numerical MHD equilibria of a circular cross section with aspect ratio $R_0/a=5$, and two specified pressure profiles. For these two pressure profiles, the ion temperatures T_i have almost the same value near the magnetic axis, but very different temperature gradients ∇T_i, as shown in Fig. 2(a). In this region, the temperature gradient scale length is much larger than the local minor radius, $L_T/r\gg 1$. The ion collisionality parameter $\nu^{*1,2}$ ranges radially from $\sim$0.4 near the magnetic axis to less than 0.01 at the outside, falling into

the banana to banana-plateau regime in terms of conventional definitions. In terms of the local neoclassical theory, the ion thermal flux q_i is proportional to the local ∇T_i:

$$q_i \propto T_i^{-1/2} \frac{\partial T_i}{\partial r}. \tag{16}$$

This predicts, for example, at a radial location $r/a=0.05$, that the ion heat fluxes differ by a factor of >30 for the two model profiles. Our simulation results of q_i vs r are plotted in Fig. 2(b) and compared with the theoretical predictions of the Chang-Hinton formula. For the case of a significant temperature gradient [case I in Fig. 2(a)], the ion heat transport is much lower than the neoclassical level. A similar result of greatly reduced ion thermal transport was reported in earlier simulations.[5,9,23,24] However, this reduced transport is just one aspect of the physics picture. For a relatively flat temperature profile [case II in Fig. 2(a)], the ion heat flux can be much larger than the local theory prediction. The simulations obtained roughly the same q_i for the two model profiles, which is clearly decoupled from the local plasma parameters. The underlying physics is the nonlocality of ion neoclassical transport. On the other hand, moving away from the magnetic axis toward the boundary, the q_i value from the simulation agrees as expected with the theoretical prediction for both temperature profiles.

Further, it is observed that the radial extension of the nonlocal transport region becomes wider as a higher ion temperature value is used in the simulation. This indicates the correlation between the extension of the nonlocal transport region and the ion orbit size. Near the magnetic axis, the ion orbit topology changes dramatically.[23,25–27] In the region far from the magnetic axis, the conventional banana orbits have a large radial excursion of order

$$\Delta_b = 2\left(\frac{r}{R}\right)^{1/2} \rho_{i\theta}.$$

As the banana orbit width increases toward the magnetic axis, those orbits change to a "potato" shape. The potato orbits are the widest ones that exist in a tokamak geometry. The so called potato region is a core region centered at the magnetic axis with a radius defined by $r=\Delta_b$, which gives the potato width

$$\Delta_p = (2q\rho_{\mathrm{th}})^{2/3} R_0^{1/3},$$

where q is the safety factor and ρ_{th} the gyroradius of thermal ions with velocity $\sqrt{2T_i/m_i}$. In the potato region $r \lesssim \Delta_b$, there reside many unconventional ion orbits that have radial excursions comparable, or even equal to the local system size (local minor radius). Since this violates the conventional local transport description, the nondiffusive and nonlocal character is expected to become predominant in the collision-driven transport process. For the two cases of Fig. 2, the radius Δ_p is $\sim 0.17a$, which may define the strongly nonlocal transport region. In Fig. 2, the simulated ion fluxes agree, as expected, with the local transport picture at larger radii. There is a transition region between the nonlocal and local transport regions.

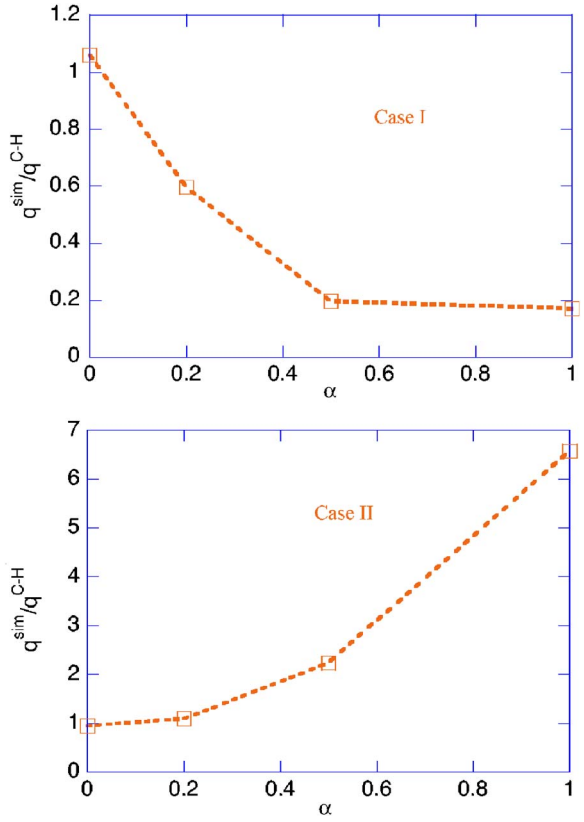

FIG. 3. (Color online) Ion heat flux (at $r=0.05$) normalized by the local neoclassical theory prediction (using the Chang-Hinton formula) scales with orbit size represented by the parameter α.

To gain a further understanding of this nonlocal transport phenomenon, we use the following numerical experiments to examine the scaling of the ion heat flux with respect to the ion orbit size. In our numerical experiments, the ion orbit sizes are artificially changed by multiplying the drift terms (containing $\mathbf{v}_d$) on the left hand side of Eq. (7) with a numerical factor α in the range $0 \le \alpha \le 1$. Roughly, ion orbit size scales with α as $\Delta = \alpha \Delta_0$, where Δ_0 is the actual ion orbit width. Note that the two limits $\alpha=0$ and $\alpha=1$ correspond to the zero orbit size of standard neoclassical theory and the true orbit size, respectively. Also note that a generalized two-weight scheme that is given in the Appendix, along with the noise reduction technique, should be used to solve the δf equation. This carefully designed simulation allows us to continuously vary the ion orbit size while keeping the essential plasma conditions, such as collisionality, unchanged. This is a useful way to obtain clear results with regard to finite orbit effects. The simulation uses the same parameters as in Fig. 2. The ion heat flux, normalized by the value of the neoclassical theory prediction, vs α (or ion orbit size) is plotted in Fig. 3, which shows that large ion orbits introduce transport nonlocality. In the zero orbit case($\alpha=0$), the result of local transport theory is recovered. As the ion orbit size is artificially increased, the heat flux diverges from the local diffusion theory. Moreover, the divergence may go in different directions, showing the dependence on the details of the T_i profile shape: for a relatively flat temperature profile enlarged ion orbits tend to increase the ion heat flux; for a

relatively significant temperature gradient, enlarged ion orbits tend to decrease the heat flux. Roughly speaking, large ion orbits tend to bring the heat flux to a certain level that depends more on the average value and the shape of the temperature profile in the region, but is decoupled from the local temperature gradient.

It is interesting and instructive to examine the contribution of ions at different energies to the total heat flux. This result of $q_{i,\mathrm{bin}}$ vs v/v_{th} is presented in Fig. 4, where $q_{i,\mathrm{bin}}$ is a velocity space distribution function of the heat flux, defined as

$$q_{i,\mathrm{bin}}(r,v/v_{\mathrm{th}}) \equiv \left\langle \int \frac{1}{2} m_i (\mathbf{v}-\mathbf{u})^2 (\mathbf{v}_d \cdot \nabla r) \delta f \mathcal{J}_{v,v_\parallel} dv_\parallel \right\rangle, \tag{17}$$

with $\mathcal{J}_{v,v_\parallel}$ the Jacobian of velocity space $(v_\parallel, v)$. It is shown that (i) ions with $v \sim 2v_{\mathrm{th}}$ make the largest contribution to the total heat flux; (ii) thermal ions with $v \sim v_{\mathrm{th}}$ make a negative contribution to q_i; (iii) in the region near the magnetic axis where transport is nonlocal, there is no significant difference in the $q_{i,\mathrm{bin}}(v)$ distribution, except that it slightly shifts to the lower v side.

However, as shown in Fig. 5, there exists a significant difference in the ion heat distribution function $q_{i,\mathrm{bin}}(r,\lambda)$ between the region near the magnetic axis and the outside region. In the outside region, ions in the range of $-0.5 < \lambda < 0.5$ make a dominant contribution to the heat flux, while the other ions' contribution is very small. This is consistent with the conventional picture that, in the low collisionality regime (banana to banana-plateau), trapped ions, which have a large radial excursion, carry most of the heat flux. In the region near the magnetic axis, where the ion transport is nonlocal, the heat flux is carried by ions that are located in a narrow range of the λ space, centered at $\lambda \sim -0.25$, while ions with positive values of λ make almost no contribution to the heat flux. As the position moves outward, the nonzero heat flux in λ space is gradually extended in the positive λ direction. For case I and case II of Fig. 2, this heat flux distribution in λ space is rather similar, while the nonlocality may either decrease or increase the ion heat transport near the magnetic axis, relative to the local neoclassical transport level.

The neoclassical equilibrium distribution function $\delta f(r, v/v_{\mathrm{th}})$ plotted in Fig. 6 also reveals a qualitative distinction between the near-magnetic axis and outer regions. This flux surface-averaged equilibrium distribution function δf shows a roughly odd parity in v space with a null point $(\delta f = 0)$ at around $v_c \sim 1.2 v_{\mathrm{th}}$. In the outer region, $\delta f > 0$ for $v > v_c$ and $\delta f < 0$ for $v < v_c$. However, a reversed pattern in δf is shown in the region near the magnetic axis where the ion transport is nonlocal. There is a transition region in between, which separates the local and nonlocal transport regions. This remarkable distinction may be instructive for further theoretical understanding of the nonlocal properties of the ion transport. On the other hand, experimentally, it was

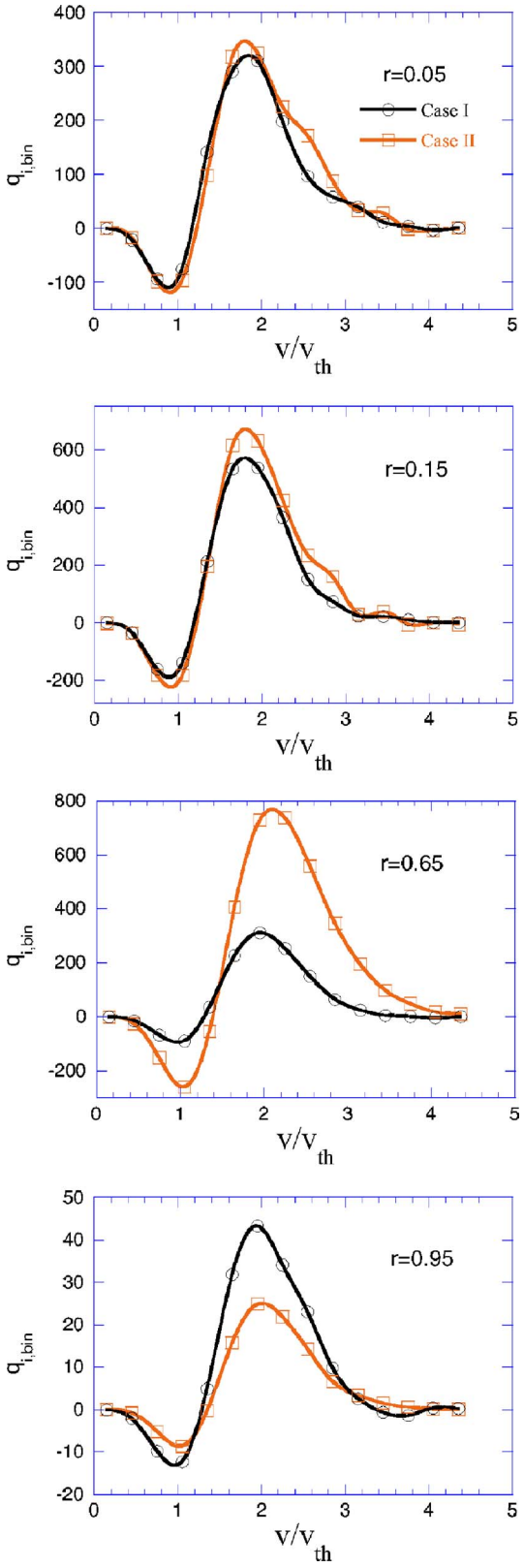

FIG. 4. (Color online) Ion heat flux distribution function: Contributions to the heat flux from ions with different energies.

observed in the ATC tokamak that the parallel-moving ion distribution function was dramatically different from that of antiparallel ions at a location $r/a = 2/3$.[28] The fat banana orbit width in the energy range where the measurement was

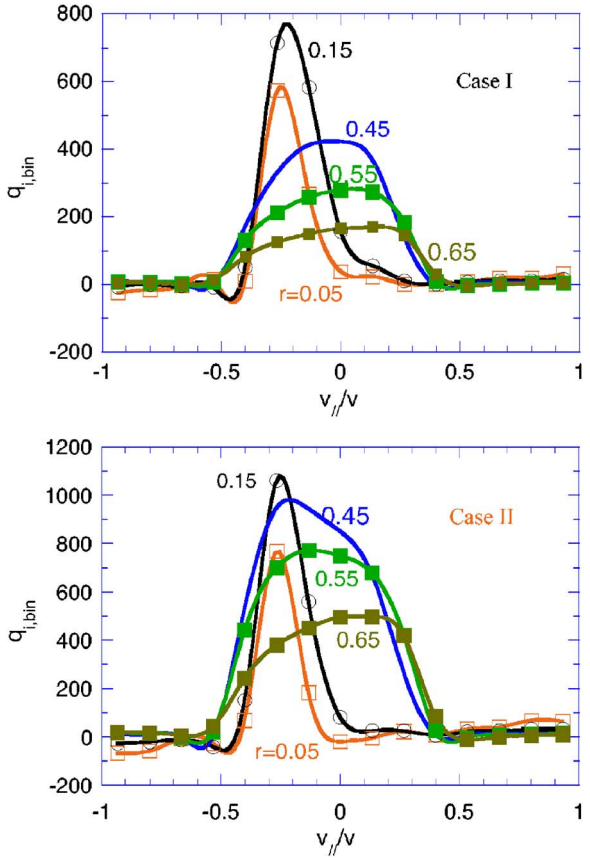

FIG. 5. (Color online) The distribution of heat flux as a function of the pitch angle variable $\lambda = v_{\parallel}/v$ of particle velocity.

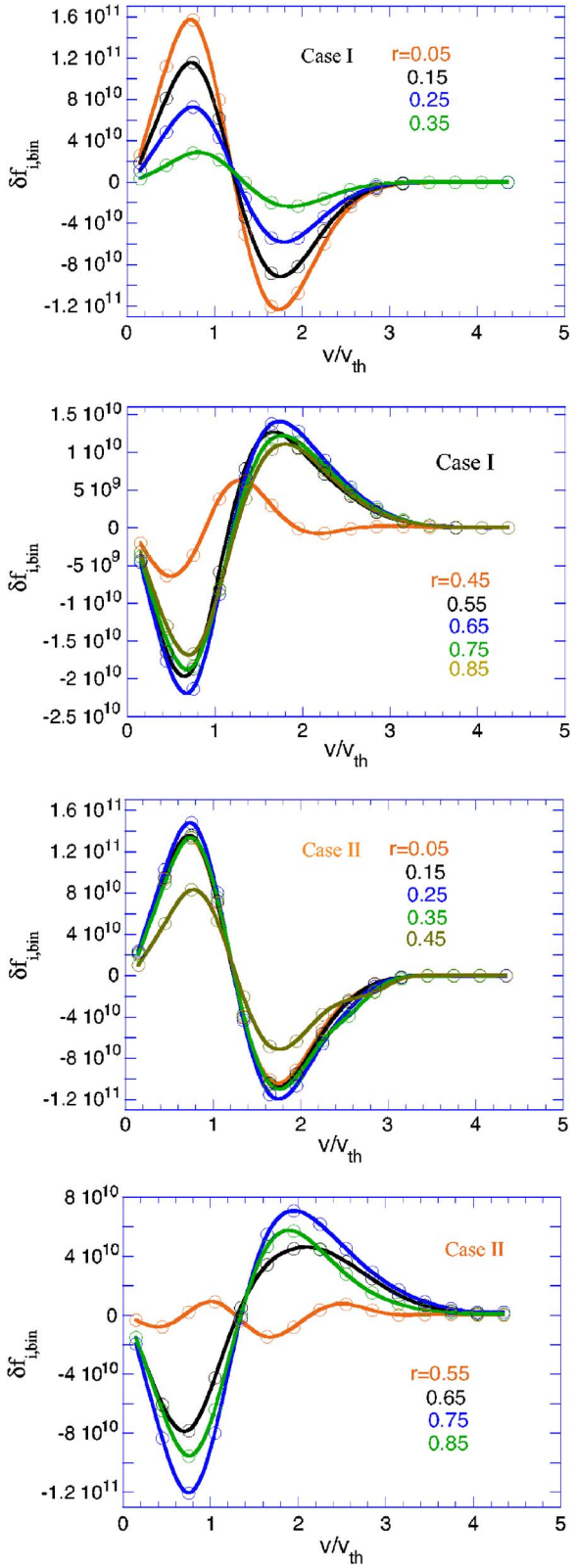

FIG. 6. (Color online) Neoclassical equilibrium distribution function with reduced dimension $\delta f(r, v/v_{th})$.

made is of the order of the minor radius. It was suggested that this measured asymmetry in the ion distribution function was due to the neoclassical effect of large ion orbits. Since this type of measurement may provide a direct test for a large-orbit neoclassical calculation with finite orbit effects at a very fundamental level, it is useful to examine the numerical distribution function associated with the experimental observations. Accordingly, a high resolution neoclassical distribution function in multidimensional phase space will be examined in future simulations.

Similar numerical experiments to those in Fig. 2 have been carried out for shaped axisymmetric magnetic configurations including NSTX geometry, which have demonstrated that the nonlocal property in ion neoclassical transport exists, in general, in NSTX plasmas. Next, we apply our simulation to examine the neoclassical properties of NSTX experiments. Figure 7 shows the result for a high-β (volume-averaged β=35%), high-density H-mode NSTX discharge. There is a reversed local ∇T_i near the magnetic axis. Correspondingly, the local transport theory (from the NCLASS code[29]) predicts an inward ion heat flux in the region. Due to the nonlocal effect associated with large ion orbits, our simulation still predicts an outward ion heat flux, which is in the same direction as the experimental measurement. Another observation associated with the finite orbit effect in the simulation is that the simulated ion heat flux shows extra "nonlocal smoothing" in the profile. Figure 8 shows another example of an NSTX discharge with a stair-step type T_i profile. For a wide range of NSTX discharges, nonlocal effects generally bring the simulated ion heat transport into closer agreement with the experimental measurements.

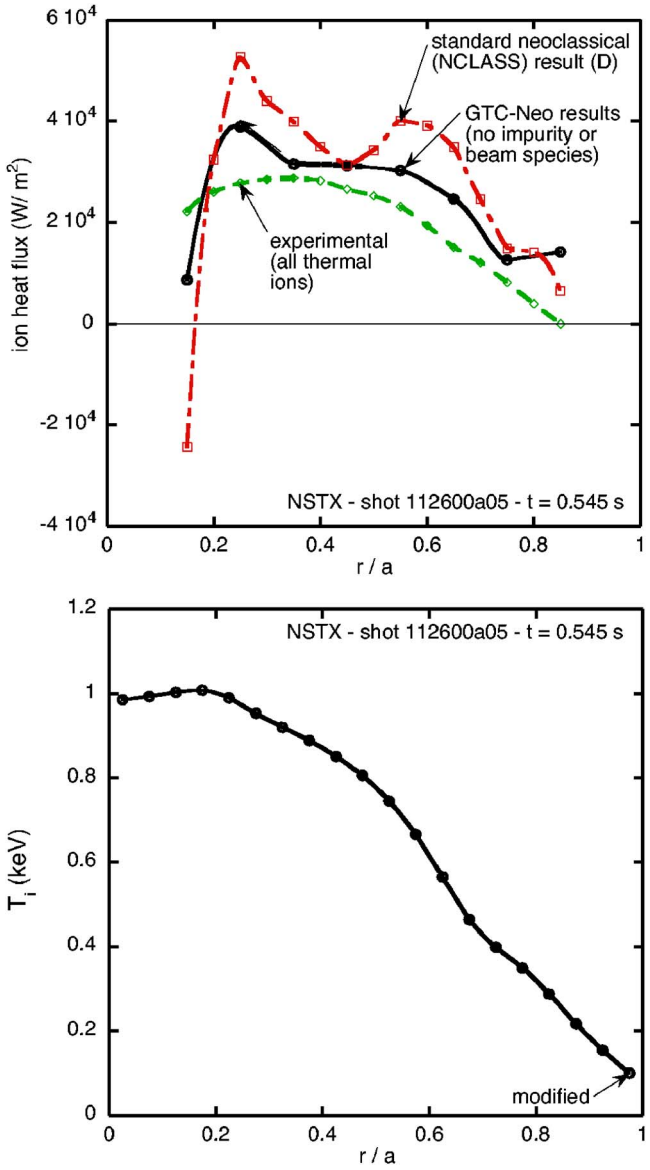

FIG. 7. (Color online) Simulated neoclassical ion heat fluxes versus r of an NSTX plasma, compared with the experimental measurement (from TRANSP modeling) and the prediction of standard neoclassical theory (from NCLASS; Ref. 29). Also plotted is the measured ion temperature profile.

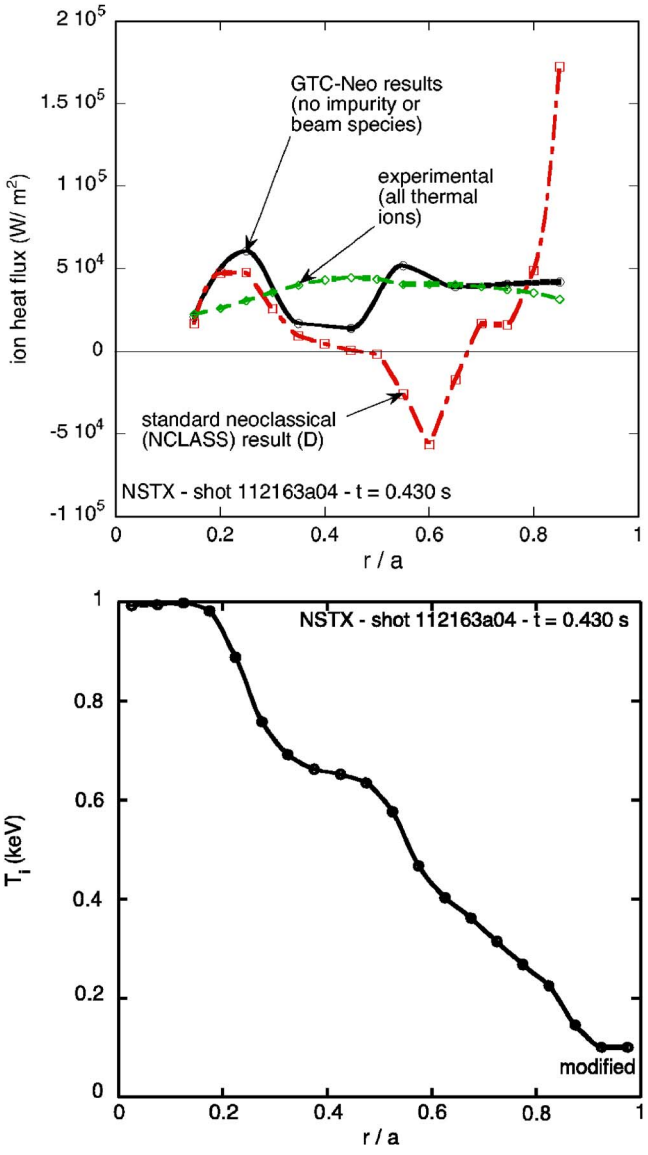

FIG. 8. (Color online) Simulated neoclassical ion heat fluxes versus r for an NSTX shot, compared with the experimental measurement and the prediction of standard neoclassical theory.

$$\langle j_b B\rangle = e\langle n(u_{i\|} - u_{e\|})B\rangle, \tag{18}$$

IV. FINITE ORBIT EFFECTS ON BOOTSTRAP CURRENT

One of the most important predictions of neoclassical theory is the bootstrap current, a noninductive current driven by the pressure gradient in a toroidal plasma, which is believed to play an essential role for the steady state operation of tokamak reactors. As present tokamak experiments with improved confinement often have edge or/and internal transport barriers with steep pressure gradients and strongly driven plasma flow, it is useful to study how the neoclassical prediction of the bootstrap current is modified by a steep plasma pressure gradient and by large toroidal rotation. Because the total bootstrap current includes the small difference between ion and electron parallel flow, expressed as any finite orbit effects that modify ion parallel flow, such as large pressure gradients, sheared toroidal rotation, and orbit squeezing effects of sheared radial electric fields, may modify the bootstrap current. On the other hand, finite orbit corrections to the electron part are negligible. In addition, there is a geometry effect that changes the trapped particle fraction.

We first study the bootstrap current in rotating plasmas. In terms of standard small-orbit neoclassical theory, the bootstrap current is independent of toroidal rotation. Recently, it has been found that sheared toroidal rotation can drive an additional parallel flow for the ions. In a toroidal plasma with uniform temperature, a quasiequilibrium solution for the distribution function for rotating ions can be constructed. In this case, this additional parallel flow can be estimated as

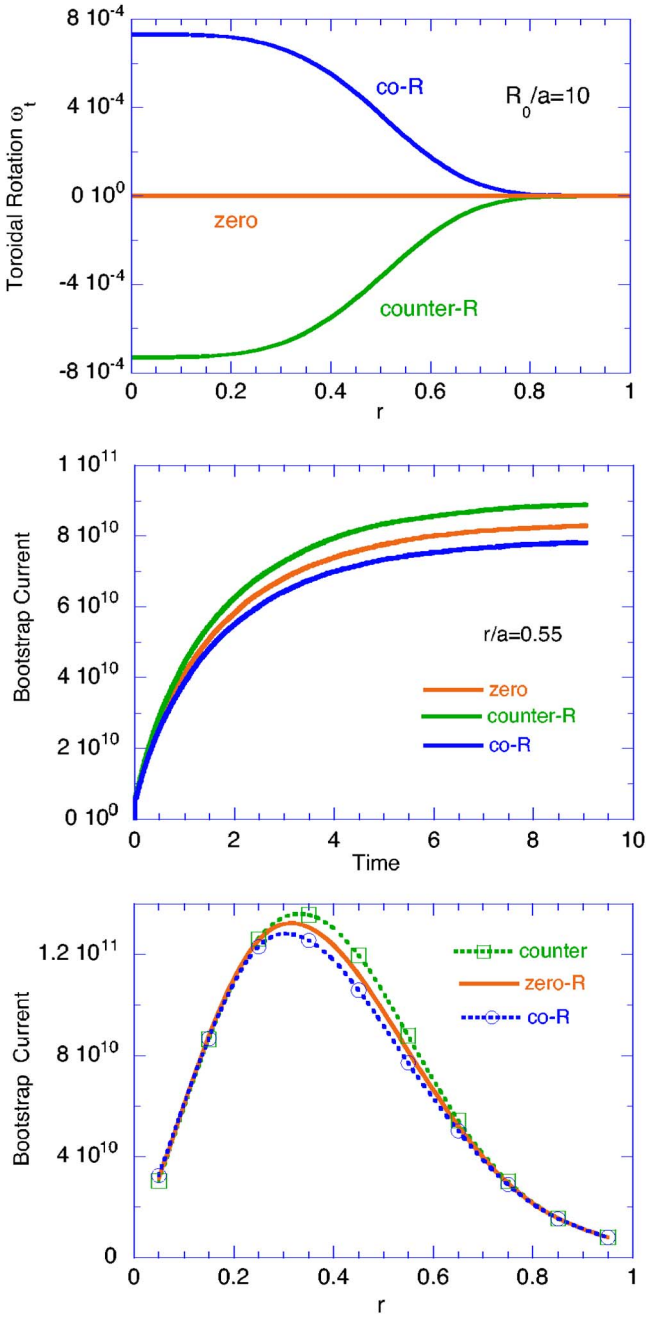

FIG. 9. (Color online) Bootstrap current in toroidally rotating plasma. Simulations use three different rotation profiles ω_t.

$$\Delta u_{i\|} \simeq -\frac{m_i c}{e}\left\langle \frac{I^2}{B^2}\right\rangle \frac{cT_i I}{eB}\frac{\partial \ln n_i}{\partial \psi_p}\frac{\partial \omega_t}{\partial \psi_p}. \tag{19}$$

Correspondingly, an additional bootstrap current is driven in a sheared rotating plasma. This bootstrap current can be either in the co- or counter-direction, depending on the direction of the rotation gradient.

Our simulation has observed, for the first time, this additional bootstrap current driven by the sheared toroidal rotation, along with the density gradient. Here we perform three simulations with different values for the toroidal rotation, as shown in Fig. 9. In two cases a strong rotation gradient exists in the region $0.3<r/a<0.65$, with the maximum ratio of the banana orbit width to the rotation gradient length $\Delta_b/L_{\omega_t}\sim 0.4$. The rest of the parameters for the three simulations are identical. The time history of the bootstrap current shows that a very clean result is obtained. The neoclassical steady state is reached in about 5–10 collision times that is related to the collisionality. In the steady state, a higher (lower) bootstrap current is observed in the region $0.3<r/a<0.65$ where there exists strongly sheared toroidal flow with $d\omega_t/dr>0$ $(d\omega_t/dr<0)$. A positive shear $(d\omega_t/dr>0)$ is favorable as it enhances the bootstrap current. On the other hand, a strong rigid rotation near the magnetic axis does not change the bootstrap current. It is also confirmed that the toroidal rotation alone, without an ion pressure gradient, cannot drive the bootstrap current. Notice that this additional bootstrap current appears to be, typically, $<10\%$ of the conventional pressure gradient driven bootstrap current.

We next study finite orbit effects associated with steep pressure gradients on the bootstrap current. Generally, a steep pressure gradient is formed in the H-mode edge plasma and in the core plasma with internal transport barriers. Here, we set up a large ion temperature gradient in the core area $0.35<r/a<0.75$, as shown in Fig. 10(a); we also assume no toroidal rotation, excluding the effect of the rotation gradient drive discussed previously. The radial profile of the simulated neoclassical electric field E_r is plotted in Fig. 10(b). The slow relaxation in the E_r profile, shown in the period from $t=1500$ to $t=7000$ (in units of the time step), may relate to the angular momentum transport driven by the temperature gradient.[17] Compared to the estimate from the standard neoclassical result for ion parallel flow, there exists a considerable difference in E_r in the region of large ∇T_i. This is equivalent to saying that the neoclassical ion parallel flow is considerably modified in the same region, which implies, as we discussed in the beginning of the section, a modification to the bootstrap current. Indeed, as shown in Fig. 10(c), the total bootstrap current (the sum of electrons and ions) is increased by around 10% in the large ∇T_i region relative to the small-orbit theory prediction of Eq. (14). On the other hand, a steep density gradient, unlike ∇T_i, is found to have little effect of modifying the bootstrap current.

Following the calculation for the heat flux distribution in terms of particle energy in the last section, it is interesting and instructive to calculate the bootstrap current distribution as a function of the particle parallel velocity to see the contributions of particles of different velocity. We define

$$\langle j_b B\rangle_{\rm bin}(r,\lambda) \equiv -e\left\langle B\int v_\| \delta f_e \mathcal{J}_{v,\lambda}\, dv\right\rangle, \tag{20}$$

and

$$\langle j_b B\rangle_{\rm bin}(r, v_\|/v_{\rm th}) \equiv -e\left\langle B\int v_\| \delta f_e \mathcal{J}_{v,v_\|}\, dv\right\rangle, \tag{21}$$

where $\mathcal{J}_{v,\lambda}$ and $\mathcal{J}_{v,v_\|}$ are the Jacobians for the velocity space (v,λ) and $(v,v_\|)$, respectively. The radial profile of the total bootstrap current and its velocity space distribution functions are presented in Fig. 11, which uses an NSTX-like magnetic geometry and plasma parameters in the simulation. Note that

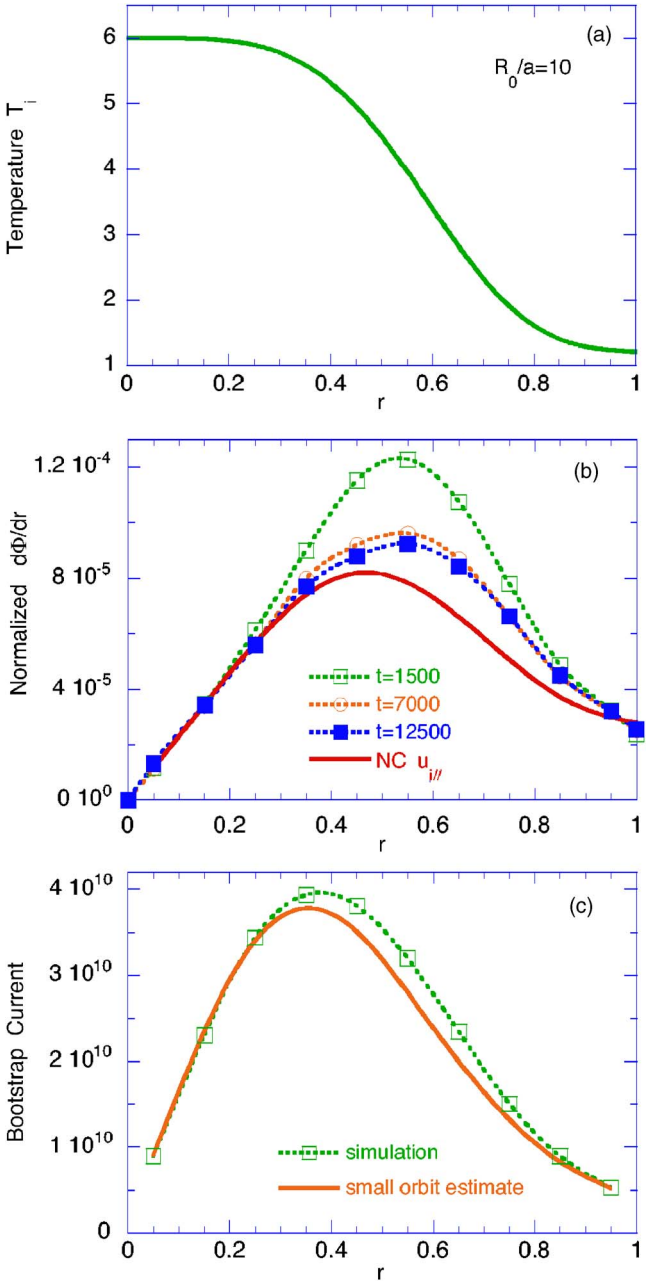

FIG. 10. (Color online) Bootstrap current with large ion temperature gradient.

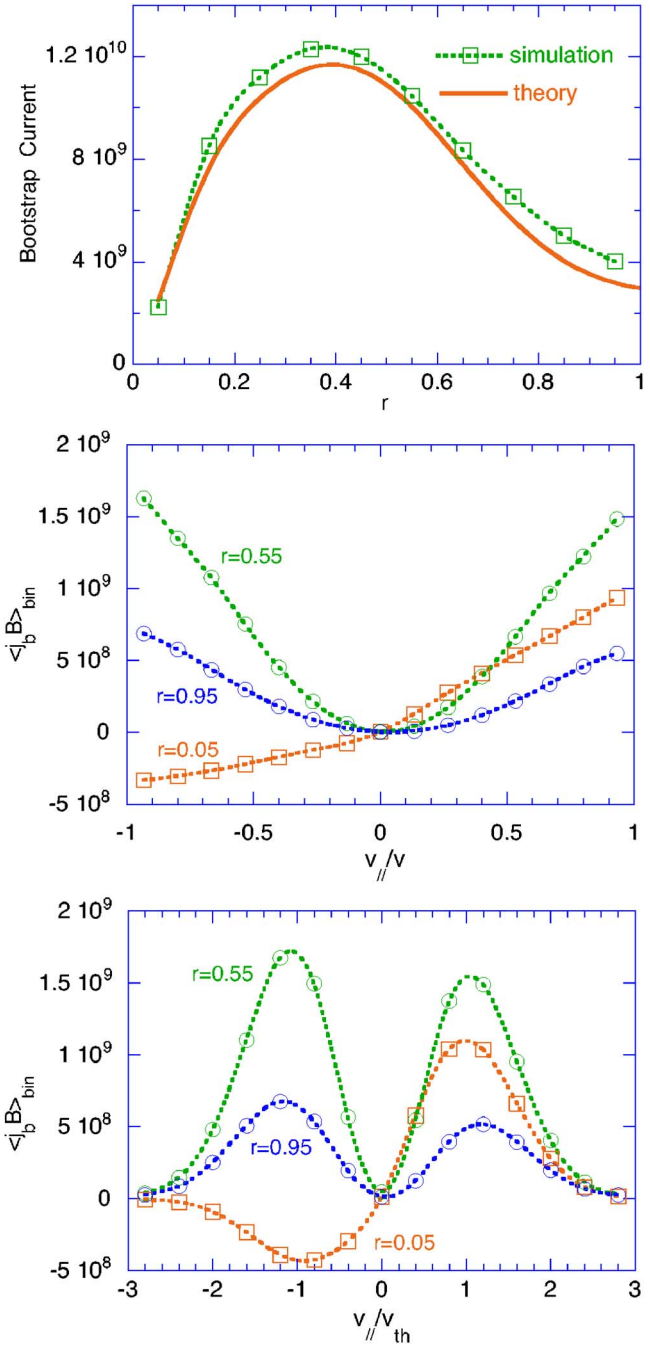

FIG. 11. (Color online) Bootstrap current $\langle j_b B\rangle$ versus r, and bootstrap current distribution as a function of the pitch angle variable λ and as a function of parallel velocity. Simulation uses an NSTX-like magnetic geometry.

only the δf part of the bootstrap current $j_b(\lambda)$ is shown here. The f_0 part of $j_b(\lambda)$ is canceled by its counterpart $j_b(-\lambda)$, resulting in no net contribution from f_0 to the total bootstrap current. These simulations confirm the expected results that the bootstrap current is dominantly carried by the passing particles (particles with a small pitch angle). Even though it relies on the existence of toroidally trapped particles, it is their collisional equilibration with the passing particles that gives rise to the bootstrap current. In terms of parallel velocity, particles with $|v_\parallel| \sim v_{\text{th}}$ carry most of the bootstrap current. These studies also reveal a significant distinction between the region near the magnetic axis and the rest of the plasma. In contrast to the other regions, near the magnetic axis, particles with $v_\parallel < 0$ make a negative contribution to the current, which almost cancels the positive contribution from particles with $v_\parallel > 0$, resulting in a small net bootstrap current in the region.

V. RADIAL ELECTRIC FIELD WITH FINITE ORBIT EFFECT

In tokamak experiments, the radial electric field can be determined by using the radial force balance relation and the measurements of toroidal and poloidal flow velocities and

the pressure profile. The radial force balance equation is expressed as

$$E_r = \frac{1}{ne}\frac{\partial p}{\partial r} + \frac{1}{c}(B_p V_T - B_T V_P), \tag{22}$$

which can be obtained from the perpendicular momentum equation of an ion species by neglecting smaller viscous inertial and collisional friction terms. On the transport time scale, the dynamic evolution of the radial electric field is governed by an angular momentum transport equation.[18] The radial force balance relation holds separately for both bulk ions and impurity species. In experiments, however, most of spectroscopic measurements are made for impurities such as carbon, and, thus, the impurity radial force balance is used to estimate E_r. The equilibrium kinetic theory predicts that the poloidal flow V_P is smaller than the toroidal flow V_T by a factor of the poloidal over the toroidal magnetic field B_P/B_T.[18,30] Since the measurement of poloidal flow is difficult and not available in most machines, it is usually replaced by the standard neoclassical expression. However, for large gradient regions, finite orbit effects are significant and can alter the inferred electric field profile. For instance, in toroidally rotating plasmas, the rotation gradient, along with the pressure gradient, can drive an ion poloidal flow due to finite ion orbits, in addition to the well known neoclassical poloidal flow proportional to the ion temperature gradient.

The equilibrium radial electric field can be calculated from a first-principles-based GTC-Neo simulation of neoclassical dynamics with finite orbit effects. Here we report our simulation results for E_r in NSTX experiments with bulk deuterium ions. Figure 12 presents the result for an NSTX discharge, which is a low density, reversed magnetic shear L mode with both ion and electron internal transport barriers (ITBs). Our simulation predicts a deeper E_r well right at the ITB location, compared to the E_r profile inferred from the radial force balance relation (for carbon) with the neoclassical poloidal flow. The associated $\mathbf{E}\times\mathbf{B}$ flow with a stronger shearing rate is, in general, more favorable for suppressing turbulence fluctuations and thus in forming a transport barrier. On the other hand, for the NSTX discharge shown in Fig. 8, where the toroidal rotation is expected to dominate E_r, the simulated E_r is in reasonably good agreement with the radial force balance estimate, as shown in Fig. 13. Recently, direct measurements of E_r and poloidal flow have been made in the DIII-D tokamak,[31] which can provide an experimental test for the neoclassical theory and finite orbit effects.

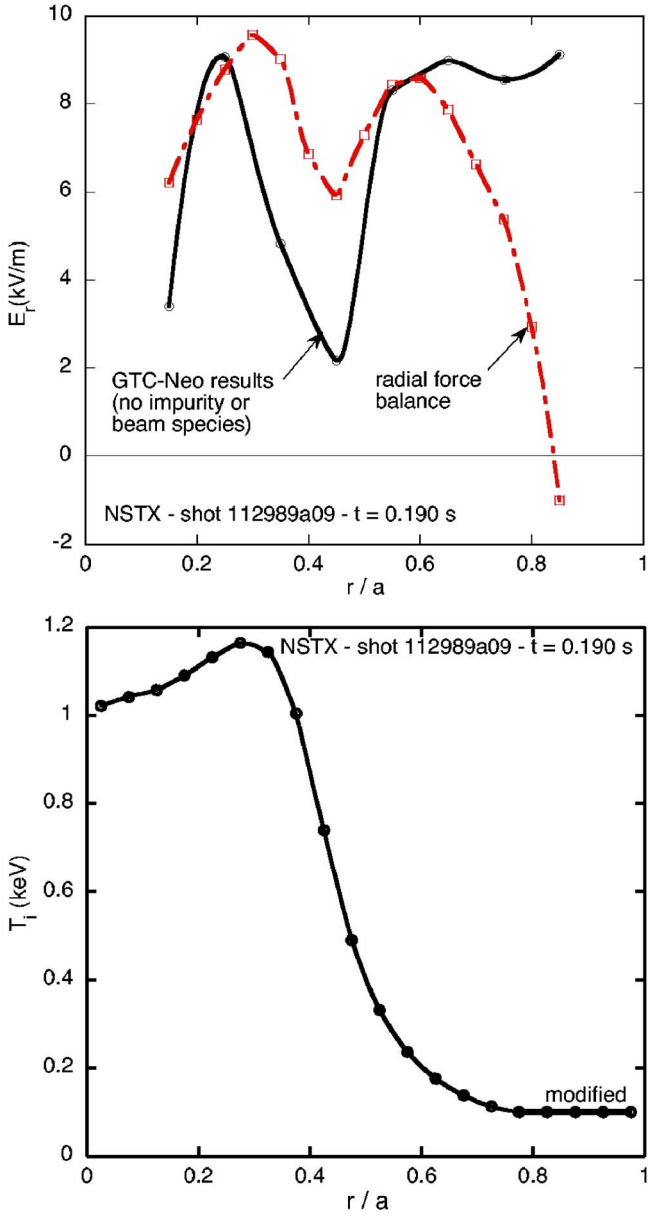

FIG. 12. (Color online) Simulated neoclassical radial electric field, compared with E_r calculated from the radial force balance relation with experimental pressure and toroidal flow velocity and standard neoclassical poloidal flow velocity.

VI. SUMMARY

Using a newly developed global δf particle simulation capability, we have investigated the nonlocal properties of neoclassical transport in tokamak and spherical torus plasmas. The verification and validation of this new computational model with respect both to analytic theory and experimental observations proved to be very encouraging. The nonlocal effects considered are associated with ion dynamics due to a large orbit size. The ion thermal transport exhibits a nonlocal nature near the magnetic axis, where ion orbits are topologically different than those in the outer radial region, and have a large size compared to the local minor radius. Specifically, the conventional linear gradient-flux relation is broken for the ion heat transport. With regard to the transport level, it can be either lower or higher than the prediction of standard neoclassical theory, depending on the details of the ion temperature profile. Correspondingly, there exists a qualitative distinction in the neoclassical equilibrium distribution function between the local and nonlocal transport regions. This distinction revealed by the simulation can be instructive for developing a theoretical understanding of nonlocal transport phenomena. We have particularly examined NSTX plasmas for which ion thermal transport is observed to be governed by the neoclassical process for many discharges. Our simulations suggest that nonlocality in ion

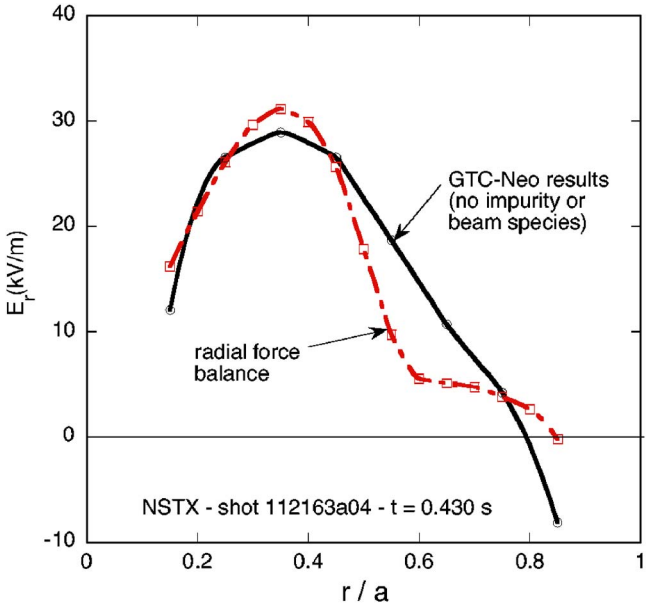

FIG. 13. (Color online) Simulated neoclassical radial electric field for NSTX discharge of Fig. 8, compared with E_r calculated from the radial force balance relation with experimental pressure and toroidal flow velocity and standard neoclassical poloidal flow velocity.

thermal transport exists for NSTX plasmas, which is consistent with experimental evidence.

The ion finite orbit effects modify the calculation of the bootstrap current via the ion parallel flow velocity. It is shown that a large ion temperature gradient can increase the bootstrap current, but a steep density gradient has little effect. When the plasma rotation is taken into account, the rotation gradient can drive an additional parallel flow for the ions and thus additional bootstrap current, either positive or negative, depending on the gradient direction. However, the modification of the bootstrap current due to finite orbit effects is hardly significant in the sense that the correction is within 20%. The reasons are that both electrons and ions contribute to the bootstrap current by roughly the same amount, and only the latter are influenced by the finite orbit effect; the bootstrap current is essentially carried by passing particles that have a smaller orbit size.

Finally, we have also reported the simulation results (for deuterium) of the radial electric field in NSTX plasmas, which, for a wide range of NSTX discharges, are generally comparable to the radial force balance result (for carbon) using measured toroidal flow and pressure profiles, and the standard neoclassical result for the poloidal flow. For an ITB case, however, our nonlocal simulation predicts a significantly larger electric field peak, at the ITB location with a steep temperature gradient. This may indicate that the poloidal flow component in E_r is significant and different from the neoclassical theory of small orbits.

ACKNOWLEDGMENTS

The authors would like to thank R. Andre, R. Budny, T. S. Hahm, G. W. Hammett, C. Kessel, W. W. Lee, Z. Lin, R. Nazikian, M. Peng, W. Solomon, S. Stutman, and E. J. Synakowski for useful discussions. The authors would also like to acknowledge R. Goldston for continued interest and discussions.

This work was supported by DOE Contract No DE-AC02-CHO-3073, and by the U.S. Department of Energy (DOE) Scientific Discovery through Advanced Computing (SciDAC) Center for Gyrokinetic Particle Simulation.

APPENDIX: GENERALIZED TWO-WEIGHT SCHEME

We present a generalized two-weight scheme in this appendix, which is used in our simulation. The δf equation to be solved is

$$\frac{\partial\,\delta f}{\partial t}+(\mathbf{v}_{\parallel}+\alpha\mathbf{v}_d)\cdot\nabla\delta f-\frac{e}{m_i}(\mathbf{v}_{\parallel}+\alpha\mathbf{v}_d)\cdot\nabla\Phi\frac{\partial\delta f}{\partial\varepsilon}$$
$$=-(\mathbf{v}_{\parallel}+\mathbf{v}_d)\cdot\nabla f_{\mathrm{SM}}+\frac{e}{m_i}(\mathbf{v}_{\parallel}+\mathbf{v}_d)\cdot\nabla\Phi\frac{\partial f_{\mathrm{SM}}}{\partial\varepsilon}$$
$$+C_{ii}[\delta f,f_{\mathrm{SM}}]+C_{ii}[f_{\mathrm{SM}},\delta f],\tag{A1}$$

where α is a numerical factor artificially introduced to control ion drift orbit size. The simulation particle distribution function $F(\mathbf{x},\mathbf{v},w,p,t)$ in the extended phase space $(\mathbf{x},\mathbf{v},w,p)$[32] is advanced according to the following kinetic equation:

$$\frac{\partial F}{\partial t}+(\mathbf{v}_{\parallel}+\alpha\mathbf{v}_d)\cdot\nabla F-\frac{e}{m_i}(\mathbf{v}_{\parallel}+\alpha\mathbf{v}_d)\cdot\nabla\Phi\frac{\partial F}{\partial\varepsilon}+\frac{\partial}{\partial\varepsilon}(\dot{w}F)$$
$$+\frac{\partial}{\partial p}(\dot{p}F)-C_{ii}[F,f_{\mathrm{SM}}]=0.\tag{A2}$$

The equations for particle weights w and p are

$$\dot{w}=\frac{1-p}{f_{\mathrm{SM}}}\left(-(\mathbf{v}_{\parallel}+\mathbf{v}_d)\cdot\nabla f_{\mathrm{SM}}+\frac{e}{m_i}(\mathbf{v}_{\parallel}+\mathbf{v}_d)\cdot\nabla\Phi\frac{\partial f_{\mathrm{SM}}}{\partial\varepsilon}\right.$$
$$\left.+C[f_{\mathrm{SM}},\delta f]\right)-\eta(w-\overline{w}),\tag{A3}$$

$$\dot{p}=\frac{1-p}{f_{\mathrm{SM}}}\left\{-(\mathbf{v}_{\parallel}+\alpha\mathbf{v}_d)\cdot\nabla f_{\mathrm{SM}}\right.$$
$$\left.+\frac{e}{m_i}(\mathbf{v}_{\parallel}+\alpha\mathbf{v}_d)\cdot\nabla\Phi\frac{\partial f_{\mathrm{SM}}}{\partial\varepsilon}\right\}-\eta(p-\overline{p}),\tag{A4}$$

where the last term on the right hand side of each equation is introduced to damp the noise,[19] with η the damping rate and $\overline{w}$ and $\overline{p}$ the average weights, defined as

$$\overline{w}=\frac{\int dw\,dp\,Fw}{\int dw\,dp\,F},\quad \overline{p}=\frac{\int dw\,dp\,Fp}{\int dw\,dp\,F}.$$

Following the same procedure given in Ref. 10, we can show that, with the two-weight scheme represented by Eqs. (A3) and (A4), the drift kinetic Eq. (A1) can be reproduced from Eq. (A2) with $\delta f=\int dw\,dp\,wF$. In the case of $\alpha=0$ (zero orbit size limit), this generalized two-weight scheme is reduced to

the linear weighting scheme.[7] In the case of $\alpha=1$, it becomes the usual two-weight scheme.[9]

[1] F. L. Hinton and R. D. Hazeltine, Rev. Mod. Phys. **48**, 239 (1976).
[2] S. P. Hirshman and D. J. Sigmar, Nucl. Fusion **21**, 1079 (1981).
[3] M. Ono, S. M. Kaye, Y.-K. M. Peng *et al.*, Nucl. Fusion **40**, 557 (2000).
[4] D. A. Gates, H. E. Mynick, and R. B. White, Phys. Plasmas **11**, L45 (2004).
[5] W. X. Wang, F. L. Hinton, and K. Wang, Phys. Rev. Lett. **87**, 055002 (2001).
[6] K. C. Shaing and R. D. Hazeltine, Phys. Fluids B **4**, 2547 (1992).
[7] A. M. Dimits and W. W. Lee, J. Comput. Phys. **107**, 309 (1993).
[8] Z. Lin, W. M. Tang, and W. W. Lee, Phys. Plasmas **2**, 2975 (1995).\
[9] W. X. Wang, N. Nakajima, M. Okamoto, and S. Murakami, Plasma Phys. Controlled Fusion **41**, 1091 (1999).
[10] W. X. Wang, W. M. Tang, F. L. Hinton, L. E. Zakharov, R. B. White, and J. Manickam, Comput. Phys. Commun. **164**, 178 (2004).
[11] R. J. Goldston, *Basic Physical Processes of Toroidal Fusion Plasmas*, Proceedings of Course and Workshop, Varenna, 1985, edited by G. P. Lampis, M. Lontano, G. G. Leotta, A. Malein, and E. Sindoni (Monotypia Franchi, Citta di Castello, 1985), Vol. 1, p. 165.
[12] J. DeLucia, S. C. Jardin, and A. M. M. Todd, J. Comput. Phys. **37**, 183 (1980).
[13] L. E. Zakharov and A. Pletzer, Phys. Plasmas **6**, 4693 (1999).
[14] F. L. Hinton and S. K. Wong, Phys. Fluids **28**, 3028 (1985).
[15] S. K. Wong and V. S. Chan, Phys. Plasmas **11**, 3432 (2004).
[16] X. Q. Xu and M. N. Rosenbluth, Phys. Fluids B **3**, 627 (1991).
[17] S. K. Wong and V. S. Chan, Phys. Plasmas **12**, 092513 (2005) (private communication, 2005).
[18] M. N. Rosenbluth, P. H. Rutherford, J. P. Taylor, E. A. Frieman, and L. M. Kovrizhnykh, Plasma Phys. Controlled Fusion **1**, 495 (1971).
[19] S. Brunner, E. Valeo, and J. K. Krommes, Phys. Plasmas **6**, 4504 (1999).
[20] R. J. Littlejohn, Phys. Fluids **24**, 1730 (1981).
[21] R. White and L. E. Zakharov, Phys. Plasmas **10**, 573 (2003).
[22] C. S. Chang and F. L. Hinton, Phys. Fluids **25**, 1493 (1982).
[23] Z. Lin, W. M. Tang, and W. W. Lee, Phys. Plasmas **4**, 1707 (1997).
[24] A. Bergmann, A. G. Peeters, and S. D. Pinches, Phys. Plasmas **8**, 5192 (2001).
[25] K. C. Shaing, R. D. Hazeltine, and M. C. Zarnstorff, Phys. Plasmas **4**, 771 (1997).
[26] P. Helander, Phys. Plasmas **7**, 2878 (2000).
[27] S. Satake, M. Okamoto, and H. Sugama, Phys. Plasmas **9**, 3946 (2002).
[28] R. J. Goldston, "Fast Ion Diagnostic Experiment on ATC: Radially Resolved Measurements of q, Z_{eff}, T_i (parallel), and T_i (antiparallel)," Ph.D. thesis, Princeton University, 1977.
[29] W. A. Houlberg, K. C. Shaing, S. P. Hirshman, and M. C. Zarnstorff, Phys. Plasmas **4**, 3230 (1997).
[30] R. D. Hazeltine, Phys. Fluids **17**, 961 (1974).
[31] W. M. Solomon, Bull. Am. Phys. Soc. **50**, 179 (2005).
[32] Y. Chen and R. B. White, Phys. Plasmas **4**, 3591 (1997).